Effective impedance of a locally resonant metasurface

M. Lott[*] and P. Roux

Université Grenoble Alpes, Université Savoie Mont Blanc, CNRS, IRD, IFSTTAR, ISTerre, 38000 Grenoble, France

We study here a mesoscopic metasurface made of a randomly distributed set of long vertical metallic rods attached to a thin elastic plate. The A_0 Lamb wave propagation is strongly affected by the local change in apparent stiffness of the plate induced by the low-quality factor resonance of the rods. At the resonance, the plate-plus-rods system is allowed to move freely, and plate waves can penetrate into the metamaterial. At the antiresonance, the plate behaves in terms of waves as if it was clamped by the rods in the metamaterial region, which induces large-frequency band gaps. Between the resonant and antiresonant frequencies, the continuous change in effective rigidity results in a continuous change in reflectivity. In the present paper, we aim at measuring the corresponding complex impedance of the metasurface in terms of amplitude and phase. Experimental data are presented to estimate the effective impedance of a locally resonant metasurface, in agreement with theoretical prediction and numerical simulation.

I. INTRODUCTION

Over the last two decades, metamaterials have shown huge potential for manipulating waves in many areas of physics [1–4]. These applications relate to electromagnetic, mechanical, and acoustic waves [5–7]. In general, the properties of these metamaterials derive from the spatial arrangement of their unitary components, whether they are ordered or not, and the nature of these components, in terms of whether they are resonant or not [8,9]. For acoustic waves, two main categories of metamaterials are classically discussed. On the one hand, the physical properties of phononic crystals can be well described by Bragg scattering. Band gaps are observed due to their periodic structure and the appropriate relationship between the wavelength and the distance between neighboring scatterers. On the other hand, disordered and locally resonant metamaterials [10–20] also show band-gap structures. However, they no longer depend on the spatial arrangement of their resonators, but on the local coupling between these resonators that leads to hybridization effects around their resonance frequency [21,22].

In acoustics, locally resonant metamaterials usually show considerable absorption loss [12], which limits their practical realization in three-dimensional (3D) systems. Moving from 3D to 2D configurations, elongated resonators can be used in one dimension with propagating waves in the orthogonal plane to the resonator axis. This can help to confine the energy, and thus to overcome part of the attenuation due to wave diffraction. These metamaterials are also defined as a metasurface in optics [23], acoustics [24], and mechanics [25]. When the 2D support medium is a thin plate, these elastic metasurfaces [26] raise new questions in terms of elastic wave interactions in a 2D + 1D physical system, where the two dimensions refer to wave propagation along the plate surface, and the one dimension corresponds to the vibration of the elongated resonators attached to it.

The main feature of a locally resonant elastic metasurface is the emergence of wide band gaps at frequencies that are much lower than for equivalent phononic crystals. Some anisotropy properties have also been reported for such metasurfaces: the design of gradient index lenses might open the route to practical cloaking applications, as they allow for the control of wave bending [27,28].

Another need for cloaking and lensing applications is a perfect match between the plate and the metasurface impedances. In practice, the impedance of a mechanical system describes the way it can transmit, radiate, or absorb elastic waves. Therefore, the measurement of the metasurface impedance requires more effort than the classical extraction of its dispersion curve [29–31]. In particular, the measurement of both the propagating and attenuating parts of the effective wave number are mandatory for the impedance calculation. The metasurface impedance is controlled by both the local rigidity and the mass of the plate, which can be affected by adding or removing some of the resonators attached to it.

The goal of the present paper is to determine the effective impedance from both the mass and stiffness variations associated to the coupled resonators in the metamaterial region. Throughout this paper, we mainly focus on two different experimental methods to extract the effective impedance of the metasurface, with consideration also of the use of numerical simulations and theoretical predictions.

To create a locally resonant metasurface, Rupin *et al.* (2014) used thin long metallic rods that were glued to an aluminum plate at the subwavelength scale with a random spatial distribution [9]. The use of rods glued to a thin plate has highlighted the symmetric and antisymmetric modal contributions of the guided waves in the plate. As will be shown later, this induces different kinds of coupling with the resonators that depend on the wave polarization [21].

———————
*martin.lott@univ-grenoble-alpes.fr

In the specific case of thin metallic plates excited at low frequency (i.e., below 10 kHz), the length of the resonators needs to be adjusted to obtain resonances in this frequency range. The present study is developed with a similar plate-plus-rods mechanical system that is excited by low-frequency Lamb waves.

This paper is organized as follows. In the following section, the experimental setup is described, along with the metasurface design and the measurement protocol. The next section deals with two experimental methods to extract the effective impedance of the metasurface. Finally, a frequency domain simulation is presented to confirm the impedance measurements, which provides further insight into the physics of such locally resonant metamaterials.

II. EXPERIMENTAL CONFIGURATION OF THE PLATE-PLUS-RODS METAMATERIAL

One hundred 61-cm-long, 6.35-mm-diameter, cylindrical aluminum rods are randomly glued over a 20 cm × 20 cm square area (which defines the metasurface) on a 6-mm-thick, 1.5 m × 2 m aluminum plate. The typical area occupied by each single rod is a 2 cm × 2 cm square. Five piezoelectric sources are used for wave generation, which are located far from the cluster of beams. The sequential transmission of an 8-s-long broadband chirp (from 1-8 kHz) from each source converts a normal force into elastic waves in the plate. The signals are then recorded at different points of the plate surface using an out-of-plane laser vibrometer that is attached to a rotating/ translating robot arm. This provides a wide (a half-disk of 60 cm) and accurate scanning area, with a spatial grid size of 4 mm. After pulse compression, the recorded signals give access to a broadband impulse response with more than 250 ms of reverberating coda due to the boundary reflections. This corresponds to an average of 125 m of propagation inside the plate.

The experimental configuration is depicted in Fig. 1. As detailed previously [9], only two modes propagate in the free plate in the frequency band of interest. With an out-of-plane displacement, the A_0 mode is vertically polarized, whereas the S_0 mode is horizontally polarized with an in-plane displacement [32]. For symmetry reasons associated to the source excitation, the dominant waves involved in this experiment are the A_0 Lamb mode. At 4 kHz, the wavelength is 12.5 cm for the free plate, and the wave speed is around 500 m/s.

III. EXTRACTING THE EFFECTIVE IMPEDANCE OF THE BEAM CLUSTER

In recent years, an analytical approach was developed to describe the physical properties of locally resonant metamaterials for Lamb waves in a plate-plus-rods system [33]. The metasurface consists of a linear periodic array of long rods that are attached to the plate that forms the substrate in which A_0 Lamb waves are excited. Using a 1D formulation, the wave propagation problem is rigorously solved by the introduction of a scattering matrix for a single rod attached to the plate, with rigorous boundary conditions at the rod/plate interface, and including both evanescent and propagating waves in the plate. Note, however, that the scattering matrix neglects the in-
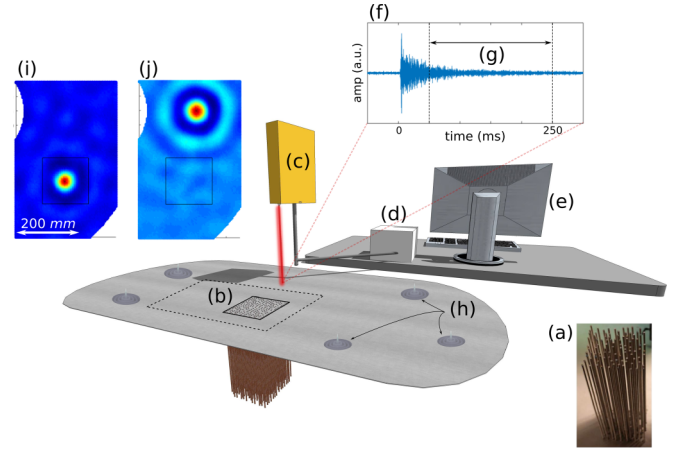
FIG. 1. Experimental setup at the laboratory scale. The metamaterial (a) is made of 100 vertical aluminum rods that are glued to the underside of a plate of the same material [(b), black square]. The particle velocity is measured using an out-of-plane laser Doppler velocimeter (c) that is connected to a PC-controlled (e) motorized robot arm (d). The recorded signal (f) is strongly dispersed due to the weak intrinsic attenuation of the plate. Using the late part of the reverberated coda (g) and a set of a few sources (h), homogeneous focal spots are reconstructed from correlations inside (i) and outside (j) the beam cluster.

plane wave-field component that is associated to the flexural resonances of the rods. To predict the transmission through the linear array of rods, the scattering matrix is used to set up an eigenvalue problem, along with the boundary conditions between the adjacent unit cells. The eigenvalues are determined precisely, and an analytical formulation can be found for the effective wave number k_{eff} within the long-wavelength approximation,

$$k_{\mathrm{eff}} = k_p \left[\frac{M_b}{M} \frac{\tan(k_b L_b)}{k_b L_b} + 1 \right]^{1/4} = k_{\Re}(\omega) + i k_{\Im}(\omega), \quad (1)$$

where k_p is the free-plate wave number, M_b is the total beam mass, L_b is the beam length, k_b is the wave number associated with the compressional motion of the beam, and M is the mass of the plate area below the beam.

Here, we are interested in the effective impedance of the metasurface, rather than its band structure. In practice, the impedance of a mechanical system describes the amplitude and phase of the local stress due to a given particle velocity value for a homogeneous medium, and it includes both elastic and viscous effects. As the experiment involves a piezoelectric disk that generates a normal force on the plate and a laser Doppler vibrometer that is sensitive to the normal particle velocity of the plate, we are looking at the following quantity:

$$Z = \frac{F_z}{v_z}. \quad (2)$$

The out-of-plane velocity generated by a normal force F_z and measured at any point distant r from the source on an infinite plate is given by [34–36]

$$v_z^p(r, \omega) = \frac{\omega F_z}{8 D k_p^2} \left\{ H_0^{(2)}(k_p r) - i \frac{2}{\pi} K_0(k_p r) \right\}, \quad (3)$$
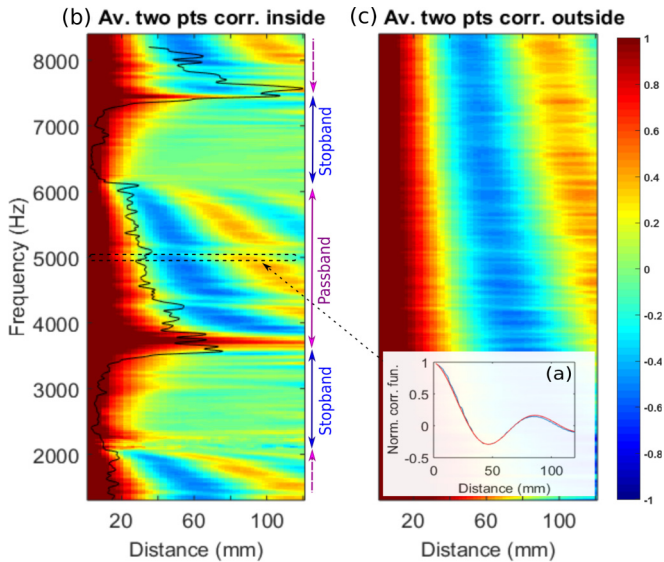
FIG. 2. (a) Real part of the averaged two-point correlation function (normalized) measured at 5 kHz for all of the receiver pairs located inside the metamaterial region (blue). The modeled plate Green's function [Eq. (3)] is in red. (b), (c) Averaged two-point correlation versus frequency measured inside the metamaterial (b) and outside the metamaterial (c). The black line in (b) corresponds to the averaged intensity versus frequency measured inside the metamaterial.

where $H_0^{(2)}$ is the Hankel function of the second kind and K_0 is the hyperbolic Bessel function. From Eqs. (2) and (3), the impedance is obtained by setting r to zero,

$$Z = 8\sqrt{Dm} = \frac{8Dk_p^2}{\omega}, \qquad (4)$$

where D is the plate rigidity, ω is the pulsation, m is the mass per unit area, and k_p are the A_0 wave numbers. In the metamaterial region, far from the flexural resonances, the polarization of the A_0 Lamb wave is conserved, and so the same impedance definition can be applied with effective parameters rather than the free-plate parameters:

$$\frac{Z_{\text{eff}}}{Z_p} = \frac{k_{\text{eff}}^2}{k_p^2}. \qquad (5)$$

The measurement of both the effective wave number k_{eff} and the free-plate wave number k_p is then sufficient for impedance estimation of the metasurface. To do so, we calculate the ensemble-averaged two-point correlation function $C(\omega, dr)$ at the pulsation ω, and for all of the possible receiving points separated by an absolute distance dr inside and outside the metamaterial region,

$$C(\omega, dr) = \frac{\langle \Psi_T(\omega, \mathbf{r}) \Psi_T^*(\omega, \mathbf{r} + \mathbf{dr}) \rangle}{\langle | \Psi_T(\omega, \mathbf{r}) |^2 \rangle}, \qquad (6)$$

where $\Psi_T(\omega, \mathbf{r})$ is the field measured from the laser vibrometer in $\mathbf{r}$ and at frequency ω for a finite-duration recorded window of duration ΔT, starting at time T. We then take advantage of the equipartition of the spatial wave field inside the plate, which was designed with an ergodic shape [20] by averaging the two-point correlation over all of the piezo
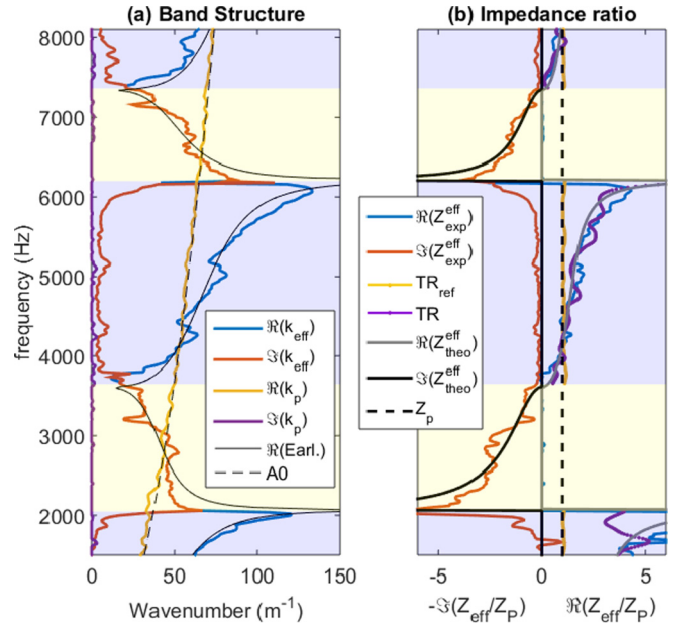
FIG. 3. (a) Metamaterial band structure. The blue and red curves (yellow and purple) are computed from the averaged two-point correlation function using Eq. (3) for the real and imaginary parts of the effective wave number, respectively, inside (outside) the metamaterial region. The black solid line shows the real part of the analytical effective wave number from Williams *et al.* (2015). The A_0 dispersion curve is plotted as a dashed line. (b) Impedance ratio obtained through different methods. Purple and yellow, from the time reversal focal spot amplitude (in the passband only); blue and red, from the two-point correlation method and using Eq. (3); black and grey, theoretical values from Williams *et al.* (2015), as the effective medium formulation and using Eq. (9). The impedance value of the free plate is plotted as the dashed line. The background colors highlight the bandwidth of the stop band (red) and passband (blue).

sources, time windows T, and vector positions $\mathbf{r}$ and $\mathbf{r}+\mathbf{dr}$. In practice, we choose $\Delta T = 10$ ms, which is small compared to the total reverberation time of the cavity, and T expands from 10 ms (for the wave mixing to be sufficient) to 250 ms (where ambient noise starts to dominate). The real part of the two-point correlation function $C(\omega, dr)$ is shown in Fig. 2(a) at frequency $f = 5000$ Hz, and in Figs. 2(b) and 2(c) for all of the frequencies inside and outside the metamaterial. In Fig. 2(a), the normalization coefficient calculated at the denominator of Eq. (6) corresponds to the averaged intensity measured from all of the receiving points inside the metamaterial (black line). As expected, passbands (where the wave field propagates inside the metamaterial) and stop bands (where almost no energy penetrates into the metamaterial) correspond to frequency bands with higher and lower averaged intensities. In the passband, the two-point correlation function is modeled as the frequency-normalized 2D Green's function for an infinite plate $v_z^p(r, \omega)$, with $k_p \longrightarrow k_{\text{eff}}$, defined as a complex number [37]. The modeled results are shown in Fig. 3(a), with the real and imaginary parts of the wave number in blue and red, respectively. In the stop band, the two-point correlation function is modeled with an effective wave number with equal
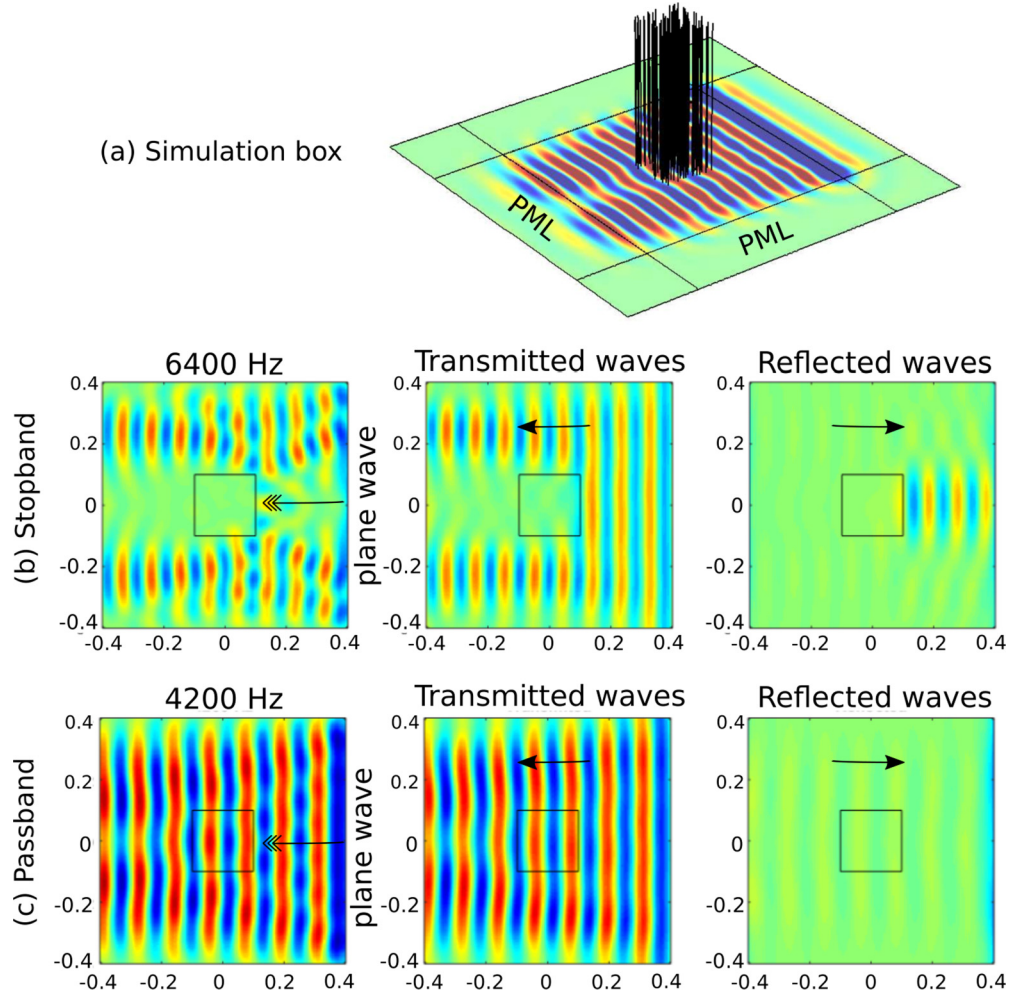
FIG. 4. Metamaterial simulation in two dimensions. (a) Simulation box: A random set of 100 beams attached to a shell component with absorbing boundaries. (b) Response at 6400 Hz, inside the stop band. (c) Response at 4200 Hz, inside the passband. The black square represents the metamaterial region. In the two left panels, the arrows indicate the incident-wave direction.

real and imaginary parts, as in Williams *et al.* (2015) [33]:

$$k_{\text{eff}} = (\pm 1 + i)\frac{k_p}{\sqrt{2}}\left|\frac{M_b}{M}\frac{\tan(k_b L_b)}{k_b L_b} + 1\right|^{1/4}. \quad (7)$$

In both the passband and the stop band, the theory is well retrieved. Note, however, an increase in the attenuation at the end of the passband. As the effective wave number strongly increases here, the wavelength becomes of the order of the average distance between neighboring rods, which results in scattering attenuation that can no longer be neglected. This scattering attenuation is not taken into account in the effective medium approximation.

The real and imaginary parts of k_{eff} are then used to calculate the impedance of the metasurface through the impedance ratio computed inside and outside the metamaterial, as shown in Fig. 3(b). The experimental results are in agreement with the theory, which is plotted as a solid line, that predicts purely imaginary impedance (equivalent to a mass) inside the band gap, and purely real impedance (equivalent to a spring) in the passband.

We use a second approach to test the theoretical prediction of the metasurface impedance only in the passband. In a shorter time than the reverberating time of the plate, and far away from the plate boundary, the average elastic strain energy (U_0) is equally distributed, because of the equipartition of the wave field [38,39]. We also assume that at the source location a normal force generates only normal velocity motion (i.e., no angular velocity) [34–36]. This means that the strain energy U_0 at the source location is only proportional to the product of the normal force F_z with the induced normal displacement u_z (also equal to $-v_z^*/i\omega$).

Then, starting from the definition of the mechanical impedance [Eq. (2)], the relative impedance between the free plate and the metasurface is accessible through the particle velocity amplitude only, and is thus directly measurable with the laser velocimeter,

$$Z(\omega, r) = \frac{F_z(\omega)}{v_z(\omega)} = \frac{F_z v_z^*}{v_z v_z^*} = \frac{-2i\omega U_0}{|v_z|^2}, \quad (8)$$

and so

$$\frac{Z_{\text{eff}}}{Z_p} = \frac{|v_z^{(m)}|^2}{|v_z^{(p)}|^2}. \quad (9)$$

For averaging purposes, an ensemble of 100 points is considered, with 50 points outside the metasurface, and 50 inside. For each point, a time-reversal focal spot is computed [Figs. 1(i) and 1(j)] by considering the long-term averaged cross-correlation of the ambient reverberating signal in the plate with neighboring points, and so simulating the virtual sources with amplitude v_z^2. We also use the five different sources in the averaging process. Then, the averaged focal spot amplitudes inside and outside the metasurface are compared. The amplitude ratio corresponds to the impedance ratio, which is plotted in purple and yellow in Fig. 3(b). The theoretical trend for the metamaterial impedance is well retrieved in the passband. In the stop band, however, the equipartition condition is no longer verified due to strong attenuation, which means that the focal spot amplitude depends on each point position within the metamaterial.

The two approaches to compute the impedance ratio are different in nature: The first is based on the wave-number extraction from the two-point correlation function, and the second is related to the amplitude of the time-reversal focal spot. In both cases, the averaging process is performed on the long-duration reverberation inside the plate and the discrete number of piezo sources. Of course, time-reversal and cross-correlation are equivalent processes. However, the wave-number extraction depends on the phase measurement between distant sensors when the time-reversal focal spot is a local measurement of the wave-field intensity. The agreement between the two approaches in the computation of the impedance shows that both amplitude and phase carry the signature of the radiated wave field from the metamaterial when equipartition is reached in the free plate.

The impedance mismatch at the interface between the free plate and the metasurface should generate transmitted and reflected waves. In a highly reverberant system, such as in the present experimental configuration, it is challenging to separate scattered waves at the metamaterial/ free-plate interface from reflected waves due to the plate boundaries. In the next section, a simulation box is designed with absorbing boundaries solely to focus on the transmitted/ reflected waves from the metasurface, as if the free plate was infinite.

IV. REFLECTION AND TRANSMISSION COEFFICIENTS: A NUMERICAL APPROACH

We use a frequency domain simulation with the COMSOL software for modeling the metamaterial components, which are based on the actual laboratory geometry. Using an incident plane wave as a source excitation [black arrows in Figs. 4(b) and 4(c), left panels], the simulation results are shown in Fig. 4 at the two frequencies, inside the stop band (6400 Hz) and the passband (4200 Hz). The wave field is filtered between the incident and reflected waves with a spatial Fourier transform. The total reflection inside the stop band and the transparency of the medium for this specific frequency inside the passband are clearly visible. This simulation provides appreciation of some of the wave-propagation effects, but it cannot be quantitative in terms of the reflection coefficient measurements. Indeed, the finite size of the metamaterial adds undesired diffracted waves at the edges of the metamaterial
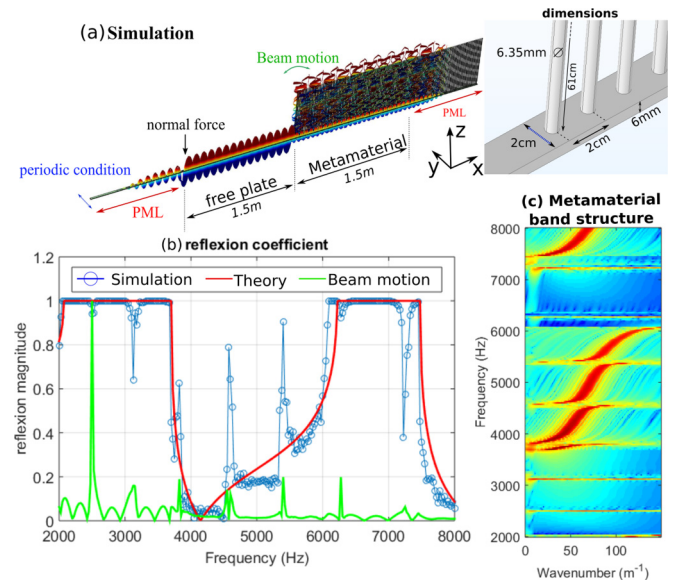
FIG. 5. Metamaterial simulation in one dimension. (a) Frequency domain simulation with lateral periodic conditions and absorbing layers at the boundaries of the medium. Inset: Metamaterial dimensions. (b) Simulation result. Blue, reflection coefficient at the beam interface calculated from the spatial Fourier transform in the free plate region; red, theoretical results obtained with Eqs. (9) and (1); green, lateral motion recorded at the top of the first beam. (c) Band structure derived from the spatial Fourier analysis of the wave field inside the metamaterial region.

region. Moreover, the randomness of the rod distribution adds some roughness effects at the metasurface interface.

To obtain a quantitative estimation of the reflection coefficient over the whole bandwidth, we choose a different approach. For plane-wave propagation, the reflection coefficient at any interface is the complex amplitude ratio between a reflected and an incident plane wave, which is also defined from the effective impedance of the two media for waves traveling from outside to inside the metasurface,

$$r = \frac{A_r}{A_i} = \frac{Z_{\text{eff}} - Z_p}{Z_{\text{eff}} + Z_p} = \frac{Z_r - 1}{Z_r + 1}, \tag{10}$$

where Z_r is the relative value (Z_{eff}/Z_p) obtained earlier, and A_r and A_i are the complex amplitudes of the reflected and incident waves, respectively. Based on the Williams *et al.* (2015) theoretical approach, the computation of the theoretical reflection coefficient is straightforward, starting with the analytical expression of Z_r [Eq. (9)].

The plate is now modeled by exploiting a 1D symmetry with a 2-m-long (x direction), 6-mm-thick (z direction), and 2-cm-wide (y direction) beam with periodic boundary conditions along the y direction. The periodic conditions help to simulate an infinite plane wave and to reduce the computational cost by limiting the metamaterial to only one line of beams. At the extremities of the plate along the x direction, two absorbing regions are added, to remove backward reflections. Within the simulation box, the only impedance mismatch is the interface between the free plate and the metamaterial region. The scheme of the simulation is shown in Fig. 5(a). Note that on the metamaterial side of the simulation

box (large x), the absorbing region is also covered with the periodic metamaterial. Indeed, without this, an impedance mismatch between the metamaterial region and the absorbing layer would be created.

The simulated wave field is analyzed through spatial Fourier transform. In the metamaterial region, the typical propagative branches and band gaps can be retrieved [Fig. 5(c)]. In the "free-plate" region, the spatial Fourier transform reveals two main peaks, one for the incident waves (positive wave number) and one for the reflected waves (negative wave number). The amplitude ratio of these two peaks provides an estimation of the modulus of the reflection coefficient R. The simulation results and the theoretical values of R are reported in Fig. 5(b) (blue and red, respectively). Once again, the Williams *et al.* (2015) theory for the effective wave number provides a good description of the metamaterial mechanical behavior. Inside the passband, the modulus of R varies from 0 to 1. Inside the band gap, however, the modulus is constant and equal to 1; this corresponds to total reflection of the wave field, which only allows evanescent waves to penetrate into the metasurface. Moreover, the reflected waves come with a frequency-dependent phase shift (not analyzed here).

As previously observed with experimental impedance measurements, simulation results show sharp perturbations at flexural resonances, compared to the Williams *et al.* (2015)

theoretical approach where in-plane wave-field components are not considered. Each flexural resonance creates a hybrid branch in the passband and wave leakage inside the stopband. In Fig. 5(b), the motion of the first beam along the x direction is shown in green. As the boundary condition at the base of each resonator evolves from "clamped" to "free" depending on frequency, we highlight here a multimodal interaction for plate waves with different polarization.

V. CONCLUSIONS

We have studied wave propagation inside a metasurface made of 100 vertical rods glued onto a thin elastic plate. Our goal was to measure the effective impedance for the beam cluster, considering both the free-plate analytical description and a recent homogenized theory for dense locally resonant metasurfaces. This theoretical approach was compared with two experimental estimations of the impedance, based on the phase and amplitude characteristics of the wave field inside and outside the metasurface. Finally, through numerical simulations performed with the same experimental configuration, the reflection coefficient is obtain for A_0 Lamb waves traveling from a free-plate region into the metasurface. These results also highlight the coupling between the orthogonal polarizations of the rod flexural resonances and the A_0 Lamb waves.

[1] J. B. Pendry, A. J. Holden, D. J. Robbins, and W. Stewart, IEEE Trans. Microwave Theory Tech. **47**, 2075 (1999).

[2] V. G. Veselago, Sov. Phys. Usp. **10**, 509 (1968).

[3] S. Yang, J. H. Page, Z. Liu, M. L. Cowan, C. T. Chan, and P. Sheng, Phys. Rev. Lett. **93**, 024301 (2004).

[4] P. Roux, D. Bindi, T. Boxberger, A. Colombi, F. Cotton, I. Douste-Bacque, S. Garambois, P. Gueguen, G. Hillers, D. Hollis *et al.*, Seismol. Res. Lett. **89**, 582 (2018).

[5] T. Ergin, N. Stenger, P. Brenner, J. B. Pendry, and M. Wegener, Science **328**, 337 (2010).

[6] A. Colombi, S. Guenneau, P. Roux, and R. V. Craster, Sci. Rep. **6**, 25320 (2016).

[7] M. Bakir, M. Karaaslan, F. Dincer, K. Delihacioglu, and C. Sabah, Opt. Eng. **54**, 097102 (2015).

[8] P. A. Deymier, *Acoustic Metamaterials and Phononic Crystals*, Vol. 173 (Springer, New York, 2013).

[9] P. Roux, M. Rupin, F. Lemoult, G. Lerosey, A. Colombi, R. Craster, S. Guénneau, and W. A. Kuperman, *World Scientific Handbook of Metamaterials and Plasmonics, Vol 2: New Trends toward Locally-Resonant Metamaterials at the Mesoscopic Scale* (World Scientific Publishing Co. Pte. Ltd., Singapore, 2017).

[10] Z. Liu, X. Zhang, Y. Mao, Y. Zhu, Z. Yang, C. T. Chan, and P. Sheng, Science **289**, 1734 (2000).

[11] I. E. Psarobas, A. Modinos, R. Sainidou, and N. Stefanou, Phys. Rev. B **65**, 064307 (2002).

[12] N. Fang, D. Xi, J. Xu, M. Ambati, W. Srituravanich, C. Sun, and X. Zhang, Nat. Mater. **5**, 452 (2006).

[13] S. Guenneau, A. Movchan, G. Pétursson, and S. A. Ramakrishna, New J. Phys. **9**, 399 (2007).

[14] V. Leroy, A. Strybulevych, M. Scanlon, and J. Page, Eur. Phys. J. E **29**, 123 (2009).

[15] M. L. Cowan, J. H. Page, and P. Sheng, Phys. Rev. B **84**, 094305 (2011).

[16] F. Lemoult, M. Fink, and G. Lerosey, Phys. Rev. Lett. **107**, 064301 (2011).

[17] F. Lemoult, N. Kaina, M. Fink, and G. Lerosey, Nat. Phys. **9**, 55 (2013).

[18] J. Christensen and F. J. G. de Abajo, Phys. Rev. Lett. **108**, 124301 (2012).

[19] Y. Achaoui, V. Laude, S. Benchabane, and A. Khelif, J. Appl. Phys. **114**, 104503 (2013).

[20] M. Rupin, F. Lemoult, G. Lerosey, and P. Roux, Phys. Rev. Lett. **112**, 234301 (2014).

[21] M. Rupin and P. Roux, J. Acoust. Soc. Am. **142**, EL75 (2017).

[22] M. Rupin, P. Roux, G. Lerosey, and F. Lemoult, Sci. Rep. **5**, 13714 (2015).

[23] N. Yu and F. Capasso, Nat. Mater. **13**, 139 (2014).

[24] B. Assouar, B. Liang, Y. Wu, Y. Li, J.-C. Cheng, and Y. Jing, Nat. Rev. Mater. **3**, 460 (2018).

[25] L. Cao, Z. Yang, Y. Xu, and B. Assouar, Smart Mater. Struct. **27**, 075051 (2018).

[26] A. Colombi, R. V. Craster, D. Colquitt, Y. Achaoui, S. Guenneau, P. Roux, and M. Rupin, Frontiers Mech. Eng. **3**, 10 (2017).

[27] A. Colombi, P. Roux, S. Guenneau, and M. Rupin, J. Acoust. Soc. Am. **137**, 1783 (2015).

[28] A. Colombi, J. Acoust. Soc. Am. **140**, EL423 (2016).

[29] D. Colquitt, A. Colombi, R. Craster, P. Roux, and S. Guenneau, J. Mech. Phys. Solids **99**, 379 (2017).

[30] T. Liu, S. Liang, F. Chen, and J. Zhu, J. Appl. Phys. **123**, 091702 (2018).

[31] A. Geslain, S. Raetz, M. Hiraiwa, M. Abi Ghanem, S. Wallen, A. Khanolkar, N. Boechler, J. Laurent, C. Prada, A. Duclos *et al.*, J. Appl. Phys. **120**, 135107 (2016).

[32] D. Royer and E. Dieulesaint, *Elastic Waves in Solids* (Springer-Verlag, New York, 2000).

[33] E. G. Williams, P. Roux, M. Rupin, and W. A. Kuperman, Phys. Rev. B **91**, 104307 (2015).

[34] F. Fahy and J. Walker, *Advanced Applications in Acoustics, Noise and Vibration* (Spon Press, London, 2004).

[35] S. Ljunggren, J. Sound Vib. **93**, 161 (1984).

[36] L. Cremer and M. Heckl, *Structure-Borne Sound: Structural Vibrations and Sound Radiation at Audio Frequencies* (Springer Science & Business Media, New York, 2013).

[37] A. Derode, A. Tourin, and M. Fink, Phys. Rev. E **64**, 036605 (2001).

[38] R. Hennino, N. Trégourès, N. M. Shapiro, L. Margerin, M. Campillo, B. A. van Tiggelen, and R. L. Weaver, Phys. Rev. Lett. **86**, 3447 (2001).

[39] G. Dassios and E. Galanis, Q. Appl. Math. **38**, 121 (1980).